

Investigation of the Effects of Surrounding Media on the Distributed Acoustic Sensing of a Helically-Wound Fiber-Optic Cable with Application to the New Afton Deposit, British Columbia

Sepidehalsadat Hendi¹, Mostafa Gorjian¹, Gilles Bellefleur², Christopher D. Hawkes³, Don White²

¹Geological Engineering, Department of Earth, Ocean and Atmospheric Sciences, University of British Columbia, Vancouver, BC, Canada

²Geological Survey of Canada, 601 Booth St., Ottawa, ON, Canada

³Geological Engineering, Department of Civil, Geological, and Environmental Engineering, University of Saskatchewan, Saskatoon, SK, Canada

Correspondence to: Sepidehalsadat. Hendi (shendi@eoas.ubc.ca), Mostafa Gorjian (mgorjian@eoas.ubc.ca)

Abstract. Fiber optic sensing technology has recently become popular for oil and gas, mining, geotechnical engineering, and hydrogeology applications. With a successful track record in many applications, distributed acoustic sensing using straight fiber optic cables has become a method of choice for seismic studies. However, distributed acoustic sensing using straight fiber optic cables is not able to detect off-axial strain at high incident angle, hence a helically wound cable design was introduced to overcome this limitation. The helically wound cable field data in New Afton deposit showed that the quality of the data is highly-highly dependent on the incident angle (the angle between the ray and normal vector of the surface) and surrounding media.

We ~~introduce~~ ~~implemented~~ ~~adapted~~ a two-dimensional new-simple-adaptation analytical ~~two-dimensional~~ approach to determine the dynamic strain of a helically wound cable in terms of incident angle in response to compressional elastic plane waves propagating through multilayered media. ~~The-This analytical method can be used to validate the choice of boundary condition for a 3D finite element model developed in this work using COMSOL Multiphysics. of cylindrical geometry of helically-wound cable that is the primary method that we are advocating for in our work, and also and~~ quickly and efficiently assess the effects of various materials surrounding a helically wound cable ~~for simple geometry, when the numerical modeling code is not accessible and the geometry is not complex.~~ Results from the ~~proposed-modified~~ analytical model are consistent compared with results from the 3D numerical modeling obtained with COMSOL Multiphysics, for scenarios corresponding to a real installation of helically wound cable deployed underground at the New Afton mine in British Columbia, Canada. ~~Results from the analytical model are consistent with numerical modeling results.~~

Our modeling results demonstrate the effects of cement quality, and casing installment on the quality of the helically-wound cable response. Numerical modeling results and field data suggest that, even if reasonably effective coupling is achieved, ~~the soft nature of the rocks in these intervals of relatively soft rock encountered at the site would result in experience~~ low fiber strains for the HWC. The proposed numerical modeling workflow would-could be applied for more complicated scenarios

(e.g., non-linear material constitutive behaviour, and the effects of pore fluids). The results of this paper can be used as a guideline for analyzing the effect of surrounding media and incident angle on the response of helically wound cable, optimizing the installation of helically wound cable in various conditions, and to validate boundary conditions of 3-D numerical model built for analyzing complex scenarios.

1 Introduction

~~A Cutting-edge fiber~~Fiber-optic technology has ~~recently~~ become popular in geophysical, mining, geotechnical, hydrological, environmental, and oil and gas applications. Fiber optic sensing offers many advantages over conventional sensors including lower price, lower weight, large-area coverage when compared to point sensors, simultaneous sensing over the entire length of the fiber optic cable, low sensitivity of glass fiber to electromagnetic radiation, and the possibility of use in harsh environments (Madjdabadi, 2016). A comprehensive literature review about the different types of fiber optic sensing technology, in terms of application, modulation and scattering of light, and polarization can be found in Madjdabadi (2016), Miah and Potter (2017), and Hartog (2018). In earth-related engineering, three main fiber optic sensing categories are commonly used: distributed temperature sensing (DTS), distributed strain sensing (DSS), and distributed acoustic sensing (DAS) (Ranjan and McColpin, 2013; Daley et al., 2013; Hornman, 2015).

Distributed Acoustic Sensing is commonly applied to measure acoustic signals in seismic applications. In this case, fiber optic cables replace conventional point sensors such as geophones and accelerometers. DAS has been used in vertical seismic profile (VSP) surveys for over 12 years (Daley et al., 2013), and is often used to monitor micro-seismicity associated with hydraulic fracturing (Hornman, 2015). In terms of environmental application, DAS has been recently used in CO₂ sequestration projects to characterize storage reservoirs and to map the progression of the CO₂ plume within geological formations (Miller et al., 2016; Harris et al., 2016). In mining, DAS-VSP was used to image steeply-dipping ore at the Kylylahti Cu-Au-Zn deposit in Finland and to provide geological information at the New Afton Cu-Au deposit in Canada (Riedel et al., 2018; Bellefleur et al., 2020).

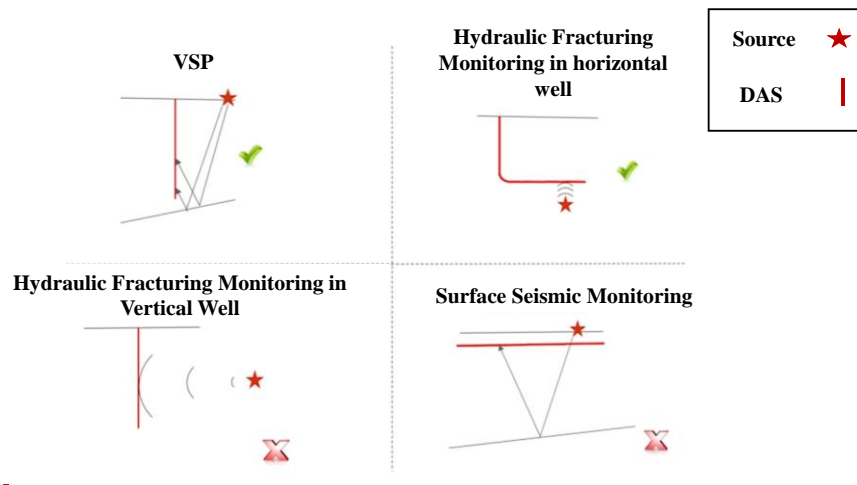
To date, most DAS applications use cables with straight optical fibers deployed in trenches at surface or in boreholes. Fiber optic cables are most sensitive to seismic waves exerting strain in the axial direction (i.e., longitudinal to the fiber) (Mateeva et al., 2014). Thus, straight fiber optic cables are only suitable for certain survey geometries (Figure 1). These include VSP applications, because the reflected compressional seismic waves propagate predominantly in a direction parallel to the fiber axis, and hydraulic fracturing monitoring, because the monitoring wells are proximal to the induced microseismic events hence the waveforms reaching the monitoring well possess sufficient curvature to generated a detectable component in the direction of the fiber axis. Conversely, DAS cannot detect seismic strain for hydraulic fracturing monitoring using vertical wells and surface seismic measurement due to a lack of resultant axial dynamic strain along the fiber optic cable (Hornman, 2015; Ning & Sava, 2016; Innanen, 2017; Eaid et al., 2018; Ning & Sava, 2018; Ning, 2019).

65 The broadside sensitivity of DAS can be improved by using helically wound fiber optic cable (HWC) (Den Boer, 2017). HWC consists of fibers wrapped around a mandrel core with a predetermined wrapping angle (α) (Figure 21). The wrapping angle controls the sensitivity of the cable, with lower wrapping angles providing higher sensitivity to broadside seismic waves. Other factors which affect HWC performance are the properties of the engineered media surrounding the cable and the coupling of these media with the rock formation (Kuvshinov, 2016). At the New Afton Cu-Au deposit in Canada, poor coupling and soft
70 formations in the immediate vicinity of the monitoring borehole caused weak seismic amplitudes in data acquired with HWC, but had minimal effects on data measured on a coincident straight fiber optic cable (Bellefleur et al., 2020). This experience illustrates the importance of understanding the effect of surrounding media on HWC in the selection and design of DAS monitoring systems.

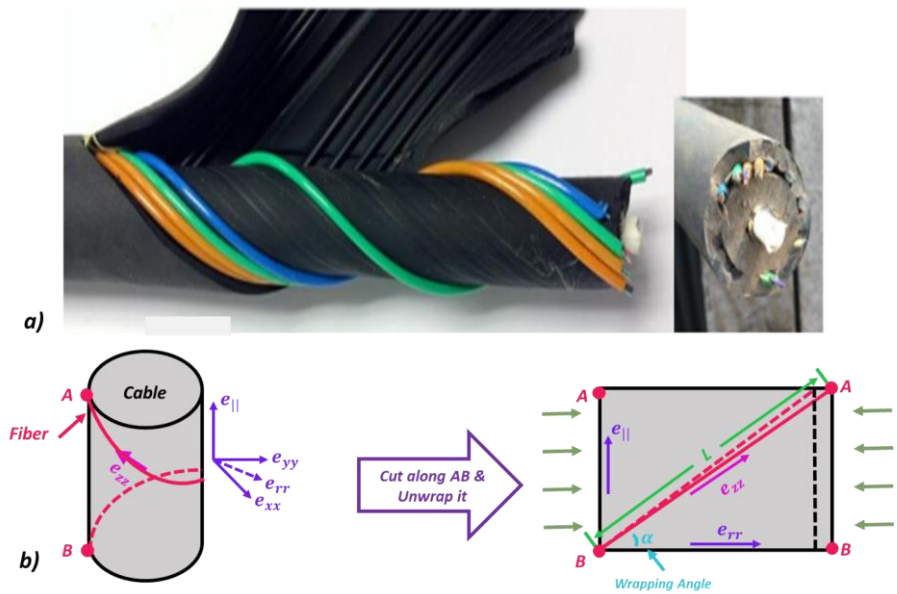
The main objectives of this work were to help address the following questions:

- 75
- Why does HWC sometimes acquire low-quality data in the field?
 - What are the effects of the surrounding media and incident angle on their impacts on cable design and installation techniques?

In order to meet these objectives, we first ~~developed~~ ~~devised~~ ~~present at the~~ ~~simple adaptation of the~~ 2-D analytical solution of
80 [Folds and Loggins \(1977\)](#) to model HWC's dynamic strain due to acoustic waves. The analytical solution provides a means of estimating HWC response using a relatively simple model that does not require specialized software. In the context of this work, the greatest value of this analytical solution was the fact that it provided a means to [validate the choice of boundary conditions of](#) ~~verify~~ a 2-D numerical model ~~that was~~ developed using the commercial software COMSOL Multiphysics. Then, having established the effectiveness of the 2-D numerical model, a 3-D model was developed using the same methods and
85 tools. Material properties and HWC geometry used for the modeling were based on the field conditions and data previously acquired during a survey at the New Afton Cu-Au deposit in Canada. [Several scenarios are modelled and compared to help identify near borehole conditions explaining the difference between data acquired with straight and HWC at New Afton, and specifically the weak-amplitude data obtained with HWC. A comparison of straight and HWC data from New Afton is presented later in the paper and used to discuss modeling results.](#) The HWC [modeling results and approach used here can](#) ~~fiber~~
90 [optic cable's output for different possible field installation scenarios was compared to provide](#) ~~provide~~ ~~insights~~ ~~fortoward~~ optimizing field deployments. Service companies could benefit by using this workflow prior to installation of HWC fiber optic cable in the field.



95 **Figure 1: Scenarios in which DAS monitoring can be effective for detecting dynamic strains include VSP's and hydraulic fracturing monitoring using horizontal wells, due to sufficient strain occurring parallel to the fiber axis. Scenarios in which DAS is less effective include hydraulic fracturing monitoring using vertical wells and surface seismic monitoring due to limitations in detecting off-axial dynamic strain (Hornman, 2015).**



100
 | Figure 21: (a) Photograph of HWC used in a trench project (from Daley et al., 2016), (b) Illustration showing the meaning of
 | wrapping angle (α). If the cylindrical surface of a cable (grey) is cut along AB, and unwrapped to a horizontal plane, the fiber
 | trajectory would be represented by the diagonal red line shown in the image on the right. The wrapping angle (α) is the angle between
 | the fiber and the circumference of the cable (BB). When a wave hits the HWC, the cable is deformed (dashed black line), and
 | accordingly the fiber is deformed (red dashed line). Dynamic strains (denoted by e) imposed on a HWC due to acoustic waves are
 | defined in an $x, y, ||$ coordinate system. (After [Kuvshinov 2016](#)[Hornman, 2015](#))
 | 105

2 Methodology

2.1 2D Analytical Modeling

110 As presented in detail in Appendix A, the wave equation was solved to determine dynamic strain as a function of incident
 | angle generated by dynamic stresses imposed by plane seismic waves propagating through a multilayered medium (after [Folds](#)
 | [and Loggins, 1977](#)). Plane waves were assumed in order to represent a point source located in the far field. Longitudinal-wave
 | properties of the materials were included in the derivation. Equations derived for this model are presented in Appendix A in a
 | form which facilitates comparison with the two-dimensional numerical simulation described later, specifically to confirm the
 | 115 boundary conditions and assumptions applied in simulation. [In appendix B, we list the pseudocode of our algorithm and](#)
 | [procedure for their implementation used in this paper are presented in appendix B. The analytical method in Appendix A is](#)

120 simpler to implement than the approach of Kushinov (2016) especially when a large number of layers are surrounding the fiber-optic cable. However, the analytical method proposed by Kuvshinov (2016) is more accurate as it evaluates cable strain in a layered cylindrical geometry. In this paper, results obtained with the simpler approach is sufficient to support and validate the choice of boundary conditions used for 3D finite element modeling (e.g. see comparison of analytical and finite element results presented later in the paper).

2.2 ~~State-of-the-Art~~ Finite Element Numerical Model

125 ~~The numerical models for this work were generated using the~~ are based on the finite element COMSOL method and were developed using the COMSOL Multiphysics software. ~~The model~~ to predicts the axial strain of a fiber as a ~~response function~~ of ~~the~~ incident angle of a compressional wave. Finite element modeling can handle the complexity of realistic geological conditions and is not subject to the simpler geometric assumptions used in analytical modeling (i.e., for instance planar or cylindrical assumptions). ~~We simulated only incident P-waves because it is the primary body wave used for exploration purposes. S-waves are seldom used for exploration and are usually removed from the seismic data during data processing (at least direct and refracted S-waves).~~ Rayleigh waves only propagate along a free surface and are not suitable source waves for the exploration of the subsurface.

130 The models were developed in the frequency domain, using a dominant frequency of 100 Hz in order to match the field ~~data~~ conditions at a site of interest (New Afton mine; see below). ~~Since the maximum response of a fiber as a function of incident angle was the main objective, simulations were~~ conducted in the frequency domain. Dominant frequency is deemed to have an effect on the transmitted energy to the fiber in an absolute sense, but ~~and~~ not on the relative magnitudes of the results generated for a range of scenarios. We do not expect significant variations in the incident angle yielding maximum response over the range of frequencies typical of seismic survey seismic frequencies.

140 Six scenarios were modeled with different combinations of mechanical properties for the materials within and around the borehole. These scenarios are listed in Table 1, and were chosen to enable assessment of the effects of various potential geometries, materials and conditions on DAS data measured with a HWC. For example, scenarios #1 and #2 compare the effect of soft and hard cement located between the casing and rock formation whereas scenarios #3 and #4 compare the effect of soft versus hard formations. Scenarios #5 and #6 investigate the effect of water located either inside or outside the casing. For this work, the geometries (Table 42) and properties (Table 23) of the materials were chosen to be similar to those of a DAS field experiment conducted at the New Afton mine, Canada (Bellefleur et al., 2020). The rock properties were based on unpublished triaxial compression testing results obtained for representative samples of crystalline fragmental volcanic host rocks at the New Afton deposit. Samples were retrieved at depths ranging from 2 to 214 m. The average values of elastic properties are presented in Table 23. The material properties related to the cable, casing and hard cement were taken from Kuvshinov (2015, 2016).

150 The six scenarios modeled. The number, and type of layers in order of proximity to the center of the cable (domains) are given in Table 1.

155

-are as follows:

Table 1. Number and type of layers (domain) implemented in numerical modeling for six scenarios. For the 2-D numerical modelling, the layers are planar. For 3-D numerical modelling, the layers are concentric, as illustrated in Figure 2.

Scenario #	Number of layers	Type of layers (in order of proximity to the center of the cable)	Figure
<u>1</u>	<u>5</u>	<u>cable, hard cement, casing, hardsoft cement and hard formation</u>	<u>2a</u>
<u>2</u>	<u>5</u>	<u>cable, hard cement, casing, soft cement and hard formation</u>	<u>2a</u>
<u>3</u>	<u>4</u>	<u>cable, hard cement, casing and hard formation</u>	<u>2b</u>
<u>4</u>	<u>4</u>	<u>cable, hard cement, casing and soft formation (soft cement)</u>	<u>2b</u>
<u>5</u>	<u>5</u>	<u>cable, they are cable, hard cement, casing, water and hard formation</u>	<u>2c</u>
<u>6</u>	<u>5</u>	<u>cable, water, casing, hard cement, and hard formation</u>	<u>2d</u>

160

- Scenario #1: this scenario is composed of 5 layers (denoted by domains). In order of proximity to the center of the cable (i.e. fiber), they are: cable, hard cement, casing, hard cement and hard formation (Fig. 3).

- Scenario #2: this scenario is composed of 5 layers. In order of proximity to the center of the cable, they are: cable, hard cement, casing, soft cement and hard formation (Fig. 3).

165

- Scenario #3: this scenario is composed of 4 layers. In order of proximity to the center of cable, they are: cable, hard cement, casing and hard formation (Fig. 4).

- Scenario #4: this scenario is composed of 4 layers. In order of proximity to the center of the cable, they are: cable, hard cement, casing and soft formation (soft cement) (Fig. 4).

- Scenario #5: this scenario is made up 5 layers: In order of proximity to the center of the cable, they are cable, hard cement, casing, water and hard formation (Fig. 5).

170

- Scenario #6: this scenario is made up 5 layers: In order of proximity to the center of the cable, they are cable, water, casing, hard cement, and hard formation (Fig. 6).

Table 2. Geometrical parameters used in numerical modeling.

Material	Geometrical parameter	Value
Cable	Cable Diameter	25.0 mm
	Cable Height	$\eta/12$ ¹
Cement/water (around the Cable)	Cement Diameter	77.8 mm
	Cement Height	$\eta/12$
Casing	Casing Diameter	88.9 mm
	Casing Height	$\eta/12$
Cement/water (around the Casing)	Cement Diameter	96.0 mm
	Cement Height	$\eta/12$
Formation	Formation Width	$\eta/12$
	Formation Height	$\eta/12$

Table 32. Layer (domain) properties used for modeling

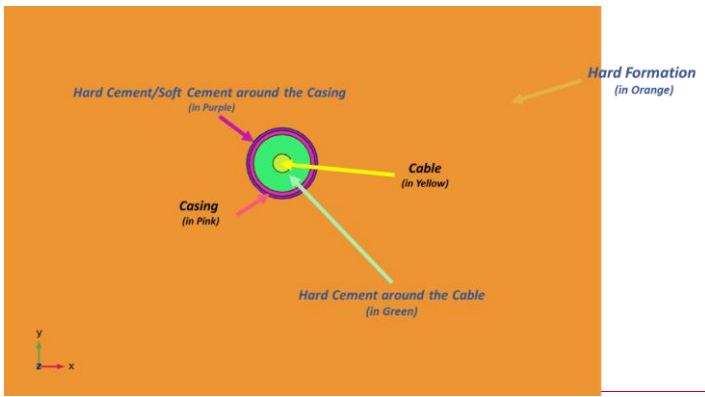
Material	ρ (kg m ⁻³)	Compressional Velocity (V_p) (m s ⁻¹)	E' ² (GPa)	ν ³
Hard Formation	2734	5736	60.1	0.28
Cable	1200	1183	1.6	0.15
Casing	8050	5635	200.0	0.28
Hard Cement	2240	2728	15.0	0.20

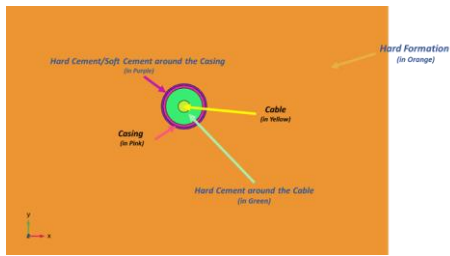
¹ $\eta = \frac{\text{(Formation Compressional Velocity)}}{\text{(Dominant Frequency)}}$

² E' is plane strain Young's modulus which is equivalent to $E/(1-\nu^2)$, where E is Young's modulus and ν is Poisson's ratio

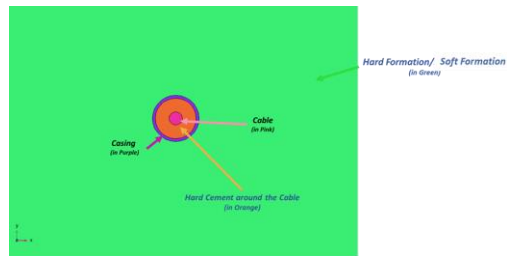
Water	1000	1500	N/A	N/A
Soft Cement/Soft Formation	1440	1963	5.0	0.20

185

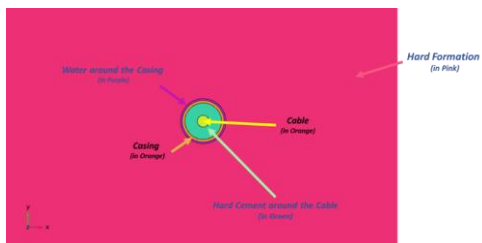




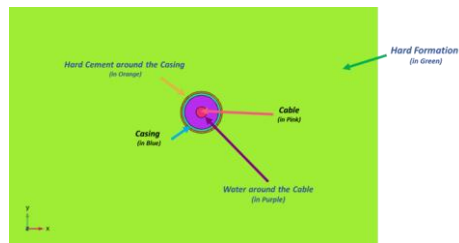
(a)



(b)



(c)



(d)

190 Fig. 32. 3-D model geometries for various scenarios, as follows: Geometry for (a) Scenario #1 and #2, (b) #3 and #4, (c) #5, (d) #6.

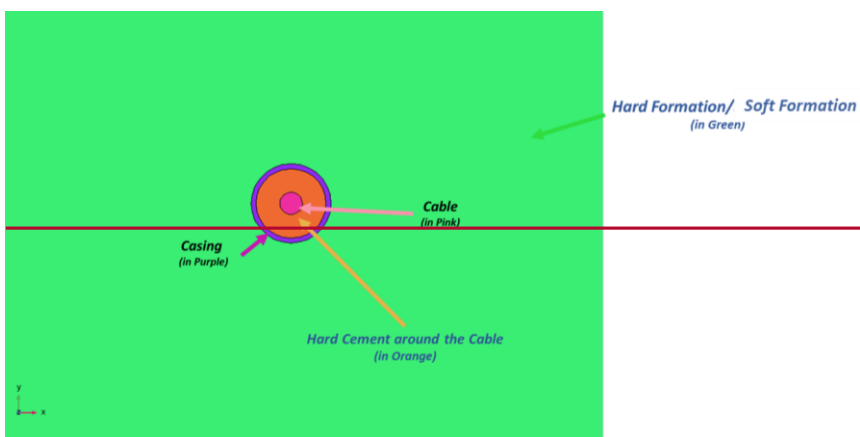
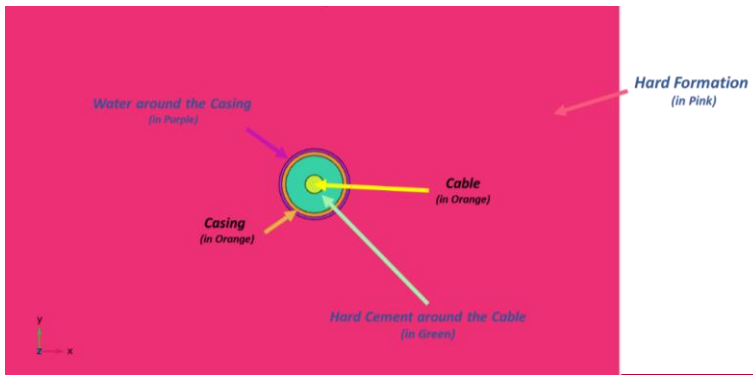


Figure 4. Geometry for scenario #3 and #4



195 **Figure 5. Geometry for scenario #5**

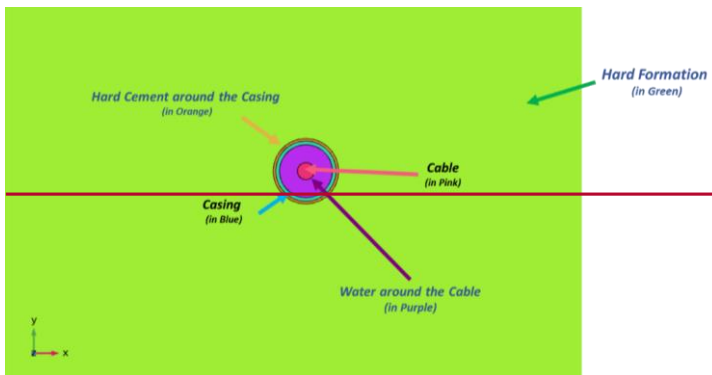


Figure 6. Geometry for scenario #6

200 In all scenarios, strain was simulated for a helically wound cable with a wrapping angle (α) of 30° (Figure 21). As shown in Appendix A (equation A.47), the longitudinal axial and radial strains of the cable were calculated separately and combined together with the wrapping angle to calculate the resultant axial strain of the fiber

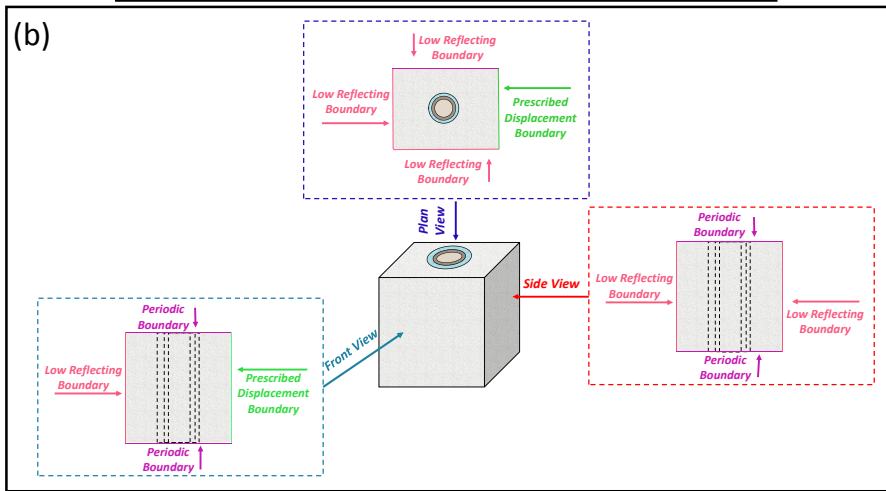
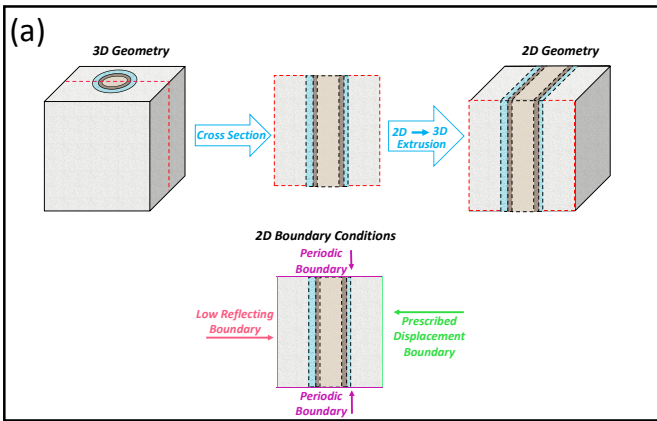
2.3 Boundary Condition for Numerical Modeling

205 In-The geometry and boundary conditions used for the 2-D numerical simulations are shown in Figure 73a. This model treats the material domains around the borehole as planar, rather than concentric. The A prescribed displacement boundary condition

was selected for the right edge of the model in order to model arrival of the incoming wave on this surface (i.e., by prescribing dynamic strains representing a wave). A low reflecting boundary was selected on the left because it is assumed there is no reflection from the adjacent semi-infinity-infinite domain. Periodic boundaries were chosen on the top and bottom boundaries to make the solutions equal on both sides.

210 The geometry and boundary conditions used for the 3-D simulations are presented in Figure 83b. They are the same as the 2-D simulation, except the material domains are concentric, centered around the cable.

▪



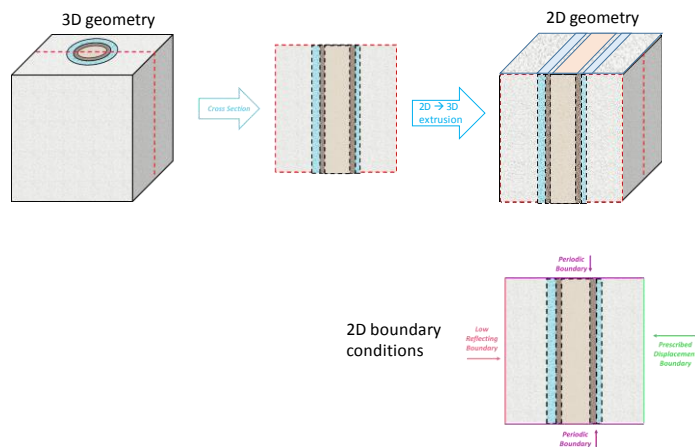
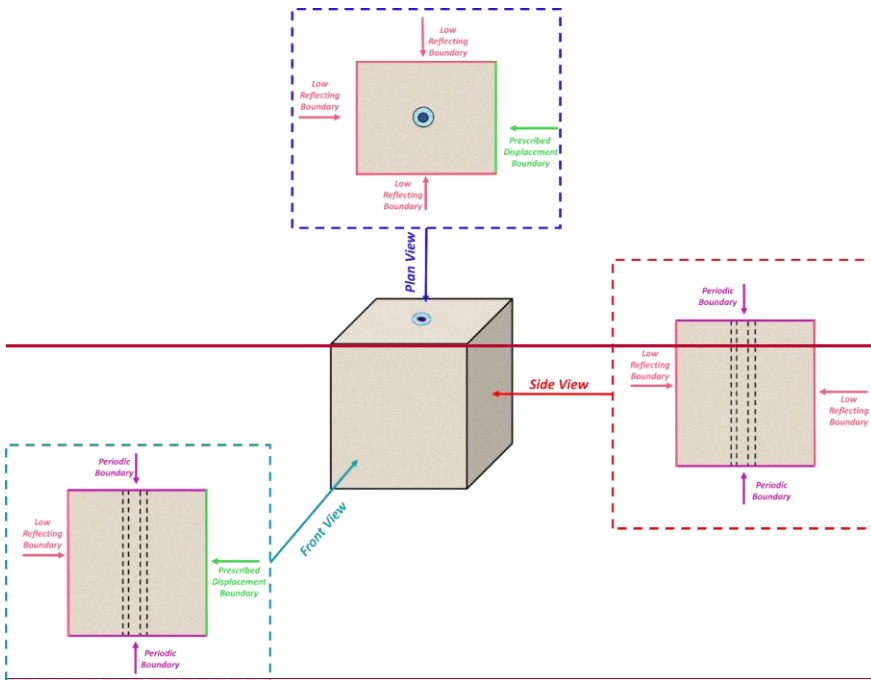


Figure 73. (a) Illustration showing how a cross-section of the actual 3-D geometry was used to create a plane-strain, 2-D numerical model, and the boundary conditions applied to this model. (b) Assigned boundary conditions for the 3-D model.



215 **Figure 8. Assigned 2-D boundary conditions from 3-D model used in this simulation.**

3 Results

3.1 Model Validation and 2D Sensitivity Analysis

220 Scenarios #1 to #4 were modeled using both the 2D analytical and numerical models in order to: (i) validate the numerical model, and (ii) to investigate the sensitivity of fiber response to cement stiffness and formation stiffness. The numerical and analytical results for scenarios #1 to #4 are presented in Figures 9-4 to 11-5. In all cases, the agreement between numerical and analytical results is good, with root mean square errors (calculated for the difference between the analytical and numerical solutions) in the 0.003 to 0.004 range. The effect of the stiffness of the cement between the rock formation and casing is shown in Figure 9-4. The analytical responses are almost identical for both scenarios whereas numerical responses differ slightly for low angles of incidence. At those angles (0-35°), fiber strain is less when hard cement surrounds the casing. The effect of the stiffness of cement around the casing becomes negligible for high angles of incidence. The effect of rock formation stiffness on fiber strain is particularly significant (Figure 10-5). The fiber strain is lower for a soft formation, modeled here using the properties of soft cement, than for a hard rock formation. This should result in a weaker seismic signal measured with DAS

225

230

for soft rock formations. Overall, responses from scenarios 1, 2, and 3 are similar, with only minor differences at low angles of incidence (Figure 11). Scenario 4 with soft rock formation properties displays the most impact on fiber strain.

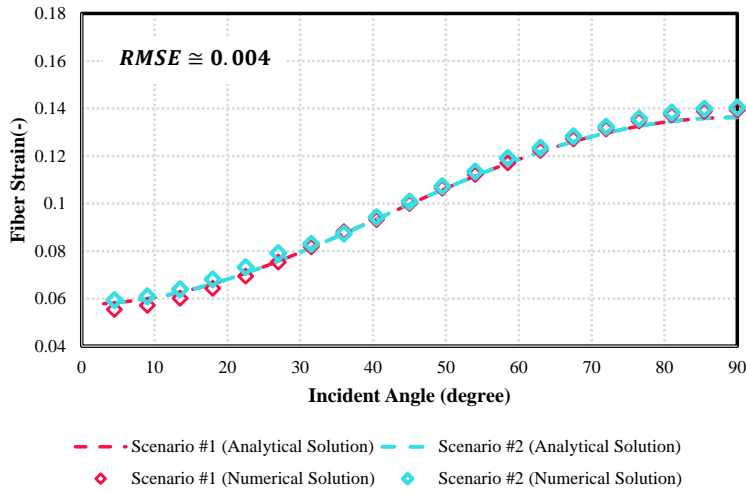


Figure 94. Axial strain for HWC fiber predicted using two-dimensional numerical model and analytical solution for scenarios #1 (cable, hard cement, casing, hard cement and hard formation) and 2 (cable, hard cement, casing, soft cement and hard formation). RMSE denotes the root mean square error calculated for the difference between the analytical and numerical solutions.

235

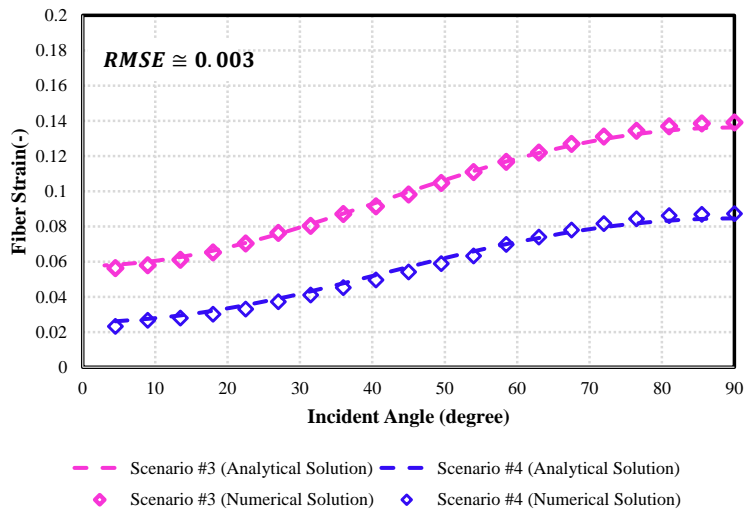


Figure 405. Axial strain for HWC predicted using two-dimensional numerical model and analytical solution for scenarios #3 (cable, hard cement, casing and hard formation) and #4 (cable, hard cement, casing and soft formation). RMSE denotes the root mean square error calculated for the difference between the analytical and numerical solutions.

240

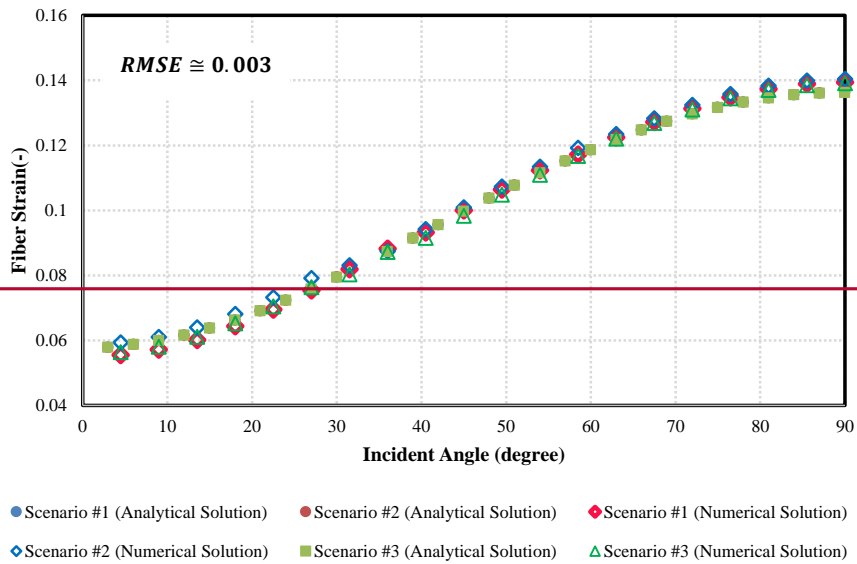


Figure 11. Axial strain for HWC predicted using two-dimensional numerical model and analytical solution for scenarios #1 (cable, hard cement, casing, hard cement and hard formation), 2 (cable, hard cement, casing, soft cement and hard formation), and 3 (cable, hard cement, casing and hard formation). RMSE denotes the root-mean-square error calculated for the difference between the analytical and numerical solutions.

3.2 3D Numerical Modeling Results

Radial strain distributions generated using the three-dimensional numerical model for scenarios 1 to 6 are shown in Figures 126-171. Those figures show the strain in all layers for a horizontal section of the 3D model, something that cannot be obtained easily with analytical methods. Axial strain results were also obtained from COMSOL and used to calculate helically wound cable strain ($\epsilon_{zz(\text{Fiber})}$) by considering a wrapping angle (α) equal to 30 degree, according to equation A.-47 (Appendix A). Scenarios with 5 layers and several thin layers (scenarios #1, #2, #5, and #6) required a significantly smaller mesh size for the simulation from in the region between the formation-casing annulus to and the cable. Though valid results were obtained, graphical rendering of strains into images for such small these finely meshed domains mesh-caused some issues, particularly for strain inside the cable. Rendered strains inside the cable for scenarios #1, #2, #5, and #6 are not displayed correctly in Figures 76, 87, 140, and 121, respectively. Strains inside the cable for scenarios #3 and #4 (Figs. 98 and 109) are properly displayed. In spite of any graphical rendering issues, all case, valid numerical strain values were obtained for all elements of the irregular mesh in all scenarios, and these results were used to produce graphs of fiber strain variations as a function of angle of incidence versus incident angle as shown in Figures 132- through 165.

260 [Figures 76 and 87](#) compare the radial strain in cases where hard or soft cement fills the casing-formation annulus. Strain in the formation for both scenarios are similar and have maximum values along the x-axis, which corresponds to the direction of the plane wave propagation. The main difference is the higher strain observed in the thin layer of soft cement between the casing-formation annulus. Strain in the casing and hard cement are, however, similar. Strain inside the cable cannot be compared for these two scenarios. The effect of having a hard or soft rock formation on radial strain is shown in [Figures 98 and 109](#), respectively. The soft formation has higher strain than the hard formation. The maximum value of strain for the soft formation, contrary to the hard formation, is distributed along the y-axis ([Figure 109](#)). This distribution of maximum strain along the y-axis is also observed inside the cable ([Figure 109](#)). The difference is particularly obvious when comparing with strain inside the cable for the hard formation ([Figure 98](#)). Also note the significantly higher radial strain inside the cable when the borehole is surrounded with a hard formation. Finally, [figures 110 and 121](#) compares the effect of having water inside the casing or outside the casing between the rock formation. The distribution of strain in the formation in the immediate vicinity of the borehole is significantly different for both scenarios with four areas of maximum strain occurring when water fills the inside of the casing. Strain in the casing-formation annulus is however larger with filled with water. For the reason mentioned above, strain inside the casing and inward cannot be compared on those figures. However, a comparison of strain as a function of angle of incidence for these scenarios is shown in [Figure 154](#).

280 [Figure 18-13](#) shows a comparison of modeled fiber strains for scenarios #1 and #2. These are identical 5-layer scenarios, except #1 assumes hard cement in the casing-formation annulus, whereas #2 assumes a soft cement in this annulus. The results are nearly identical for incident angles less than 30°. However, for greater incident angles, the scenario with soft cement in the annulus (i.e., scenario #2) is slightly more sensitive (i.e., nearly 10% greater fiber strain). This is interpreted to be due to the lower Young's modulus for soft cement, resulting in the fiber experiencing greater strain in response to an imposed dynamic stress. It should be noted that the analytical results for scenarios #1 and #2 (shown in [Figure 94](#)), showed a lesser difference between cable strain at high incident angles. A possible reason for this is because in two-dimensional analytical analysis, strain in the y-direction was considered to be zero under the plane strain assumption. In 3D, the cylindrical casing would have a slight dampening (shielding) effect on strains transmitted to the inner cement and fiber cable, but in 2D a planar "casing" would have no such dampening effect. However, results between 2D and 3D simulations cannot be directly compared quantitatively. This is explained by the fact that energy of the source plane wave and deformation occur only in the x-z plane. [The strain values from 3D finite element simulations are typically less than those obtained from 2D simulations.](#)

290 [Figure 19-13](#) shows a comparison of modeled fiber strains for scenarios #3 and #4. Both of these are 4-layer scenarios which assume that casing is in direct contact with the formation; as such, there is no casing-formation annulus. The difference between

these scenarios is the fact that #3 assumes a hard formation, whereas #4 assumes a soft formation. The results are nearly
295 identical for incident angles less than 5°, but with increasing angle scenario #3 shows a much stronger response (strains at 90°
angle nearly five times greater to #3 versus #4). For the same frequency, the wave number of the hard formation is more than
that of the soft formation. As a result, seismic energy attenuation is higher in the soft formation than in the hard formation.
Accordingly, less seismic energy is transmitted to the cable in scenario #4, compared to scenario #3, resulting in less strain for
scenario #4.

300 Figure ~~20-14~~ shows a comparison of modeled fiber strains for scenarios #5 and #6. These are both 5-layer scenarios similar to
scenario #1, except for one difference in each case. In scenario #5, it is assumed that the casing-formation annulus contains
water rather than hard cement. In scenario #6, it is assumed that the cable-casing annulus contains water rather than hard
cement. Scenario #6 shows ~~“tensile strains at low incident angles. However, the rate of increase in strain with incident angle is
relatively high compared to scenario #5, hence the compressional fiber strains for scenario #6 exceed those for scenario #5 for
305 incident angle greater than 25°, a trend of decreasing strain with increasing incident angle, up to roughly 18°.”~~ Overall, the
results show that the existence of water in the media surrounding the cable results in lower fiber strains than most of the other
scenarios. More specifically, the maximum strain (which occurs at 90° incident angle for all scenarios) is roughly 0.0065 for
scenario #5 and 0.0185 for scenario #6, compared to values in the 0.027 to 0.05 range for scenarios #1 to #3. (The only other
scenario with a comparably low strain, at 0.009, is scenario #4 which, as discussed in the previous paragraph, assumes a soft,
310 highly-attenuating formation). The low strains observed for scenarios #5 and #6 are mainly due to the interfaces between solid
and water forming a free surface, which acts to decompose incident waves into surface waves (i.e., tube waves) and
compressional waves. Accordingly, less compressional energy is transmitted to the fiber cable. Though this is true of both
scenarios #5 and #6, strains are greater in #6 because cable extension/contraction is uninhibited when the cable is within water
rather than cement.

315 Figure ~~24-15~~ shows a comparison of modeled fiber strains for scenarios #1 and #3. These are based on the same material
properties, except scenario #1 includes a cement-filled casing-formation annulus (5-layer system) whereas scenario #3 assumes
direct contact between the casing and formation (4-layer system). Both scenarios show relatively high fiber strains, with
scenario #3 having the greatest strains of all scenarios considered; and scenario #1 having the third highest (only slightly less
than scenario #2). As such, the number of layers, as a stand-alone factor, should not be expected to result in poor signal quality
320 for a HWC, assuming the layers present are hard (i.e., stiff) and well coupled.

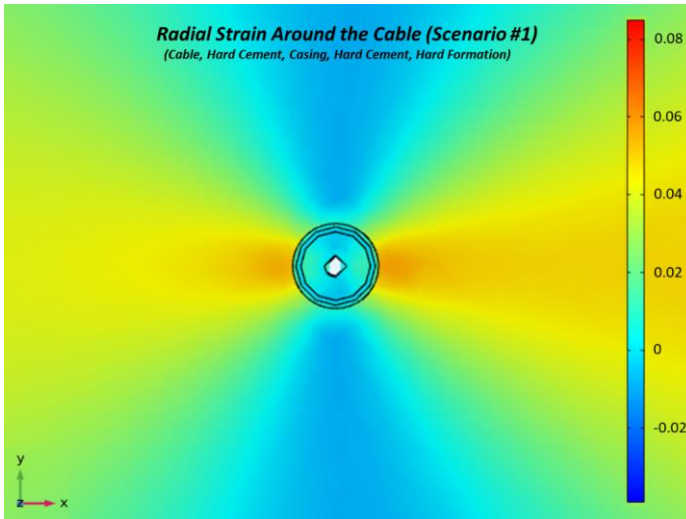


Figure 126. Radial strain around the Cable as a response of compressional wave propagation in 90° incident angle, Scenario #1 (Incident angle = 90° ; i.e., incident waveform is incoming from the right).

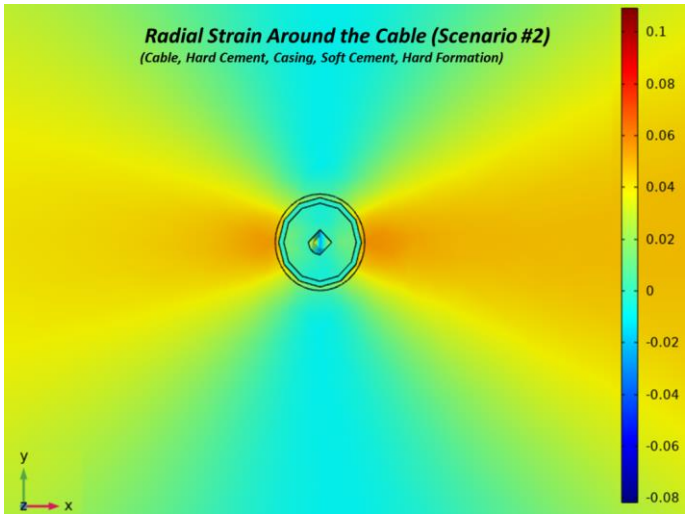
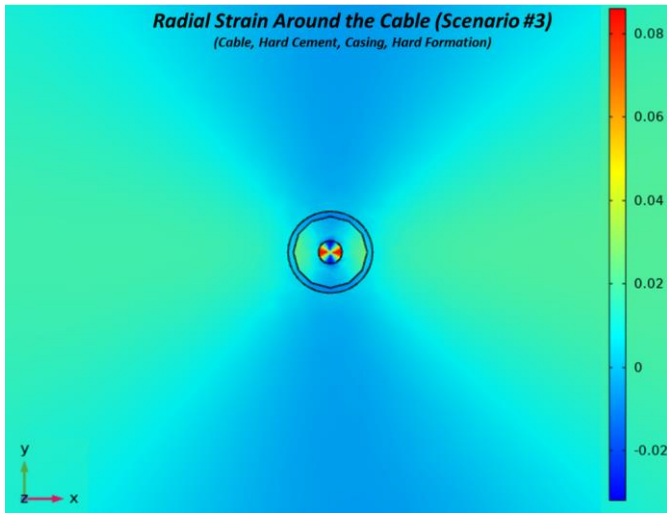


Figure 137. Radial strain around the Cable as a response of compressional wave propagation in 90° incident angle, Scenario #2 (incident waveform is incoming from the right). Radial strain around the Cable, Scenario #2 (Incident angle = 90°).

325



330 **Figure 148. Radial strain around the Cable as a response of compressional wave propagation in 90° incident angle, Scenario #3 (incident waveform is incoming from the right). Radial strain around the Cable, Scenario #3 (Incident angle = 90°).**

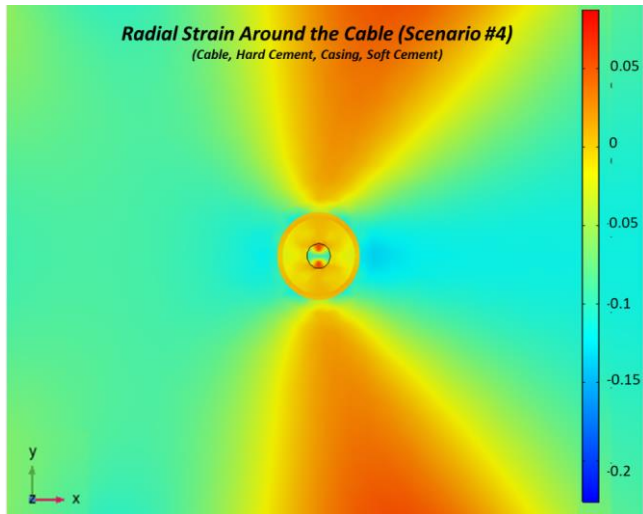


Figure 159. Radial strain around the Cable as a response of compressional wave propagation in 90° incident angle, Scenario #4 (incident waveform is incoming from the right). Radial strain around the Cable, Scenario #4 (Incident angle = 90°).

335

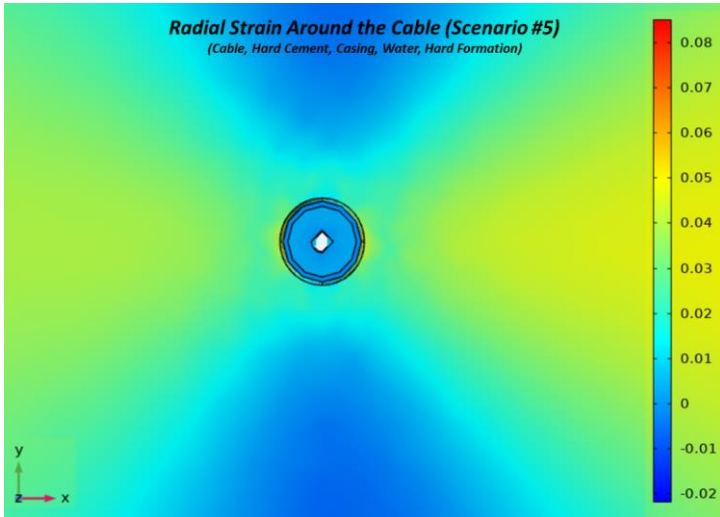
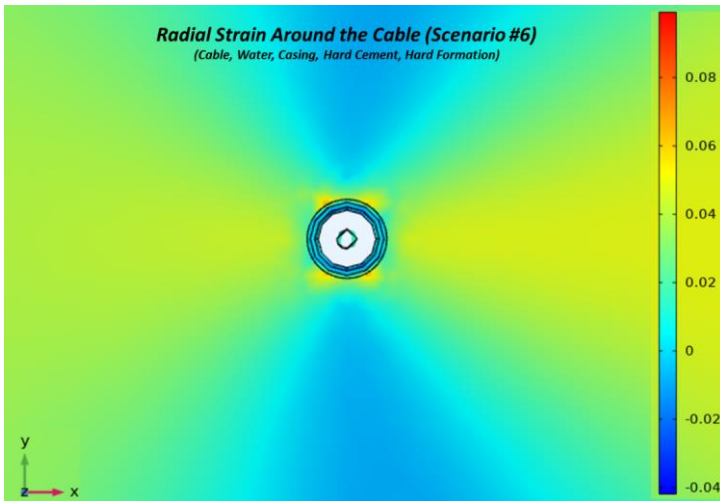


Figure 1610. Radial strain around the Cable as a response of compressional wave propagation in 90° incident angle, Scenario #5 (incident waveform is incoming from the right).Radial strain around the Cable, Scenario #5 (Incident angle = 90°).



340

Figure 1711. Radial strain around the Cable as a response of compressional wave propagation in 90° incident angle. Scenario #6 (incident waveform is incoming from the right).Radial strain around the Cable, Scenario #6 (Incident angle = 90°).

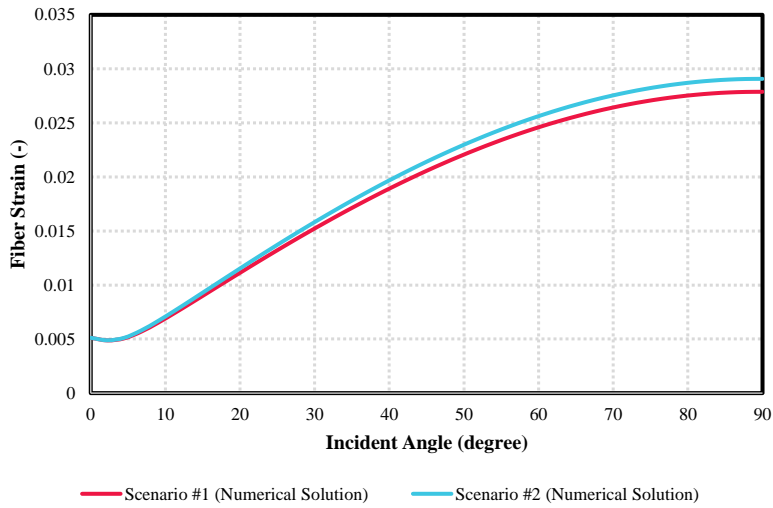
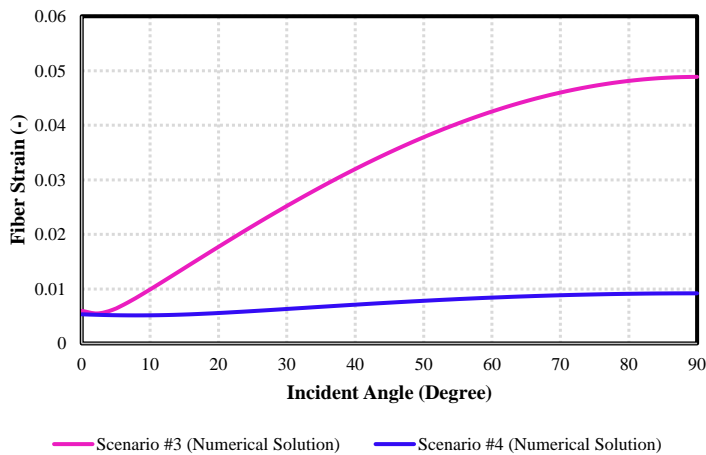
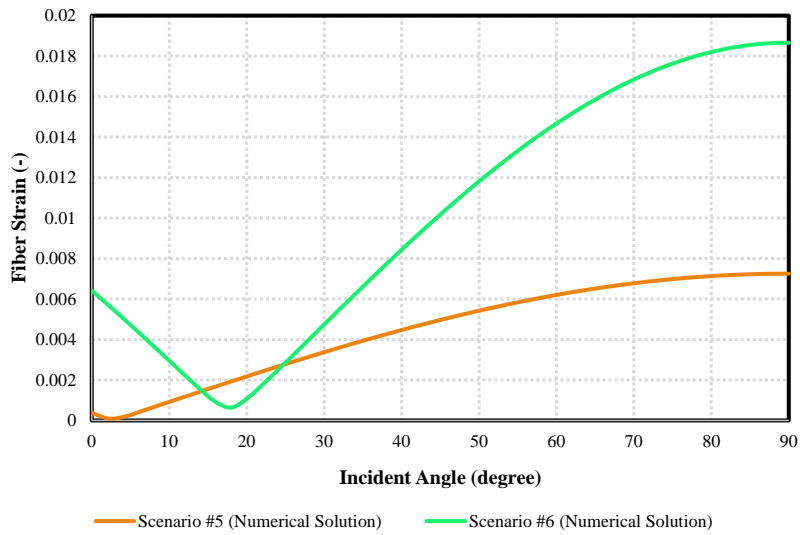


Figure 1812. Investigation the effect of cement quality (soft vs. hard) surrounding the casing on the acoustic response of fiber (comparison between scenarios #1 and #2).



345 **Figure 1913.** Investigation the effect of hard/soft Formation adjacent to the casing on the acoustic response of fiber (comparison between scenarios #3 and #4).



350 **Figure 2014.** Investigation the effect of water on the acoustic response of fiber (comparison between scenarios #5 and #6). The strain are absolute values, and the strains below 18° are tensile.

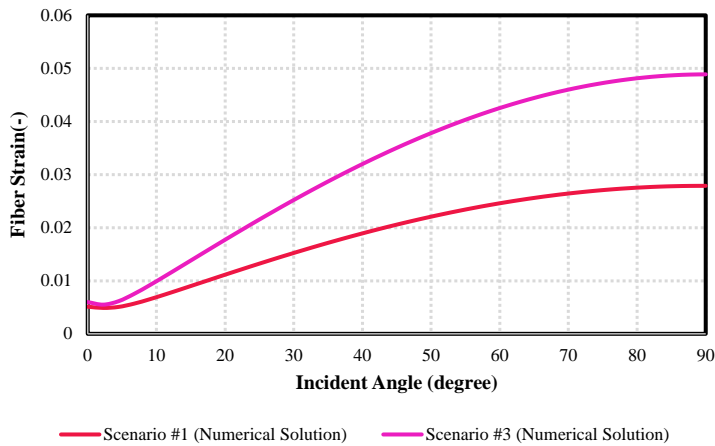


Figure 2415. Investigation the number of layers on the acoustic response of fiber (comparison between scenarios #1 and #3).

4 Discussion

The focus of this paper is on the HWC response, as however, it can apply to straight fiber optic, as well. The response of straight fiber-optic cable is well-documented in the literature (Mateeva *et al.* 2014, Kuvshinov 1996). Straight fibre-optic cable are sensitive to the axial strain. For plane P-waves, the sensitivity of a straight fibre-optic cable varies as a function of $\cos^2 \theta$, θ being the angle between the plane wave direction and the cable. A HWC is sensitive to both axial and radial strain, the latter being dependent on the material around the cable. The numerical modeling reported in this paper aims primarily at recovering the radial strain averaged over the circumference of the cable.

In this section, Here, the modeling results are used to help understand the performance of a helically-wound fiber from a field study at the New Afton mine (Bellefleur *et al.*, 2020). Figure 17622 presents a comparison of raw field VSP data acquired on collocated straight and helically wound fiber-optic cables in a steeply-dipping (70° from horizontal) deviated borehole located underground at the New Afton mine. Incident angles of seismic waves for data shown in Figure 17622 range between 25 and 40 degrees, and gauge length was 10 m for both straight and helically wound DAS data is 10 m. Due to the wrapping, strain rate over the gauge length is measured over a shorter cable distance for a helically-wound fibre than for a straight optic-fibre. This resulted in more channels for the HWC data (925 for HWC vs 813 for straight fibre-optic) for cables with identical length (828.5 m). This is an important difference between straight and helically-wound cables data shown in figure 17622 a and b. Both cables were placed inside steel drill rods (which were used as casing) and cemented in place with grout. The grout was circulated to the bottom of the borehole via a grout tube located inside the casing, and until grout eventually reached surface from both inside and outside of the casing (drill rods), after which it was allowed to. The grout cured for one month prior to

the VSP survey. Based on the afore-noted grout returns both within and outside the casing, it was assumed at the time that grout had filled both the casing and the casing-formation annulus; however, data collected during the survey (discussed below) suggests this may not have been the case.

The data were acquired with 1 kg of explosives fired in a 20 m deep shot hole at surface. An advanced DAS system providing higher signal-to-noise ratio (Carina system by Silixa) was used to record the seismic data. More details about instruments and acquisition parameters can be found in Bellefleur et al. (2020).

Our modeling results demonstrate that cementing of the helically-wound cable in hard rocks would not be detrimental to DAS measurements. Thus, cementing alone cannot explain the difference of amplitudes between straight and helically-wound cable.

Adding a thin layer of steel representing the casing also has minimal effects on modeled DAS data response.

Bellefleur et al. (2020) make the following observations and offer the following interpretations to explain them: Data recorded with the straight fiber-optic cable include several noisy traces at the locations indicated by the vertical arrows near the top-left corner of Figure 17622a; in particular near traces 90 and 215, which coincide with fault zones as identified using wireline log data. Such noise is typical of un-cemented or poorly cemented casing and is caused by local casing resonance. Noisy traces are also observed at similar locations in the HWC (see vertical arrows near the top-left corner of Figure 17622b), but resonance noise on those traces is not as strong as the straight fiber data. The HWC data are, however, strongly affected by tube waves between the two fault zones (see diagonal arrows in the left half of Figure 17622b), which suggests the presence of liquid or incomplete cementing of the casing-formation annulus. Aside from the traces showing noise and resonance, the signal strength (fiber strain) of the linear fibre appears relatively good. As shown in Figure 17622a, this dataset contains many events indicated with arrows and comprising direct P- and S-waves, many down-going waves (arrows C and D), and reflected waves (indicated with white arrows). This suggests that the cement within the casing (i.e., encompassing the fibre cables) cured properly and contained no liquid, hence enabling a strong signal in the axial direction in response to the vertical component of the propagating seismic waves. Conversely, the HWC dataset showed a relatively weak response to the afore-noted events.

Based on the results obtained in this work, and specifically on results for for which scenario #5 (water-filled casing-formation annulus), the relatively weak response of the HWC dataset suggests that cementing emplacement and curing outside of casing was not effective for a significant portion of this borehole. The results obtained in scenario #4 (soft rock formation in direct contact with casing) provide an additional explanation for poor signal quality; one which might be relevant over some intervals of the borehole. This is suggested because Bellefleur et al. (2020) noted several weak and unstable intervals, and had to ream these intervals during drilling and logging operations, and leave drill rods in place over these intervals to prevent borehole collapse during logging operations. Scenario #4 suggests that, even if the weak zone converged on the casing and achieved reasonably effective coupling, the soft nature of the rocks in these intervals would result in low fiber strains for the HWC.

The DAS dataset at New Afton, interpreted in the context of our modeling, serves as a practical demonstration of the extreme effects of surrounding media and coupling on HWC data quality. These results, and new scenarios simulated with the models developed in this work, can also be used to design more effective HWC systems in future field work.

5 Conclusion

405 We have ~~developed-employed~~ a simple adaptation of 2D analytical method to model dynamic strain generated in HWC due to plane compressional waves propagation in multilayer media. This analytical model is useful to model simple scenarios and can validate boundary conditions applied in 3D numerical model of complex scenarios. To validate the choice of boundary conditions for 3D numerical model. Strain-strain values in helically-wound fiber optic cable estimated with our analytical method are comparable-compared to those modeled with numerical simulations. Despite its inherent approximation, the comparison of results obtained the analytical approach with 3D numerical modeling and analytical approach are quite acceptable and sufficient to confirm the accuracy of selected boundary conditions. The three-dimensional finite element modeling approach used in our paper is state-of-the-art and provides all the accuracy required to model effects on fiber optic cable for complex and realistic geological situations. We have investigated the effects of the surrounding media on the axial and radial strains of HWC for six scenarios representative of realistic situation and based on parameters of DAS experiment

415 conducted at the New Afton deposit, British Columbia. Based on our parameters, our ~~analytical and 3D~~ numerical results show that the quality of cement (hard vs soft) between the casing and rock formation has a moderate effect on HWC data, with lower strain values observed for hard cement. However, having fully cured and emplaced cement inside and outside of casing is crucial to acquire decent signal from HWC. Effects of rock formation (hard vs soft) is more significant and can contribute to signal reduction on DAS data for HWC placed in soft rock formation. -In all scenarios, effects are largest at higher incident angles (i.e. 90°). ~~Presence-The presence~~ of a water domain in the surrounding materials would make the fiber response more complicated owing to the combined effect of compressional and surface waves (i.e. tube waves).

420 Interface between water domain and solid domain acts as a free surface. When a head wave hits this interface, some part of energy converts to surface waves (tube waves) and the other part as compressional wave. Fluid does not support shear waves.

Conflict of interest

425 The authors know of no conflicts of interest with this publication.

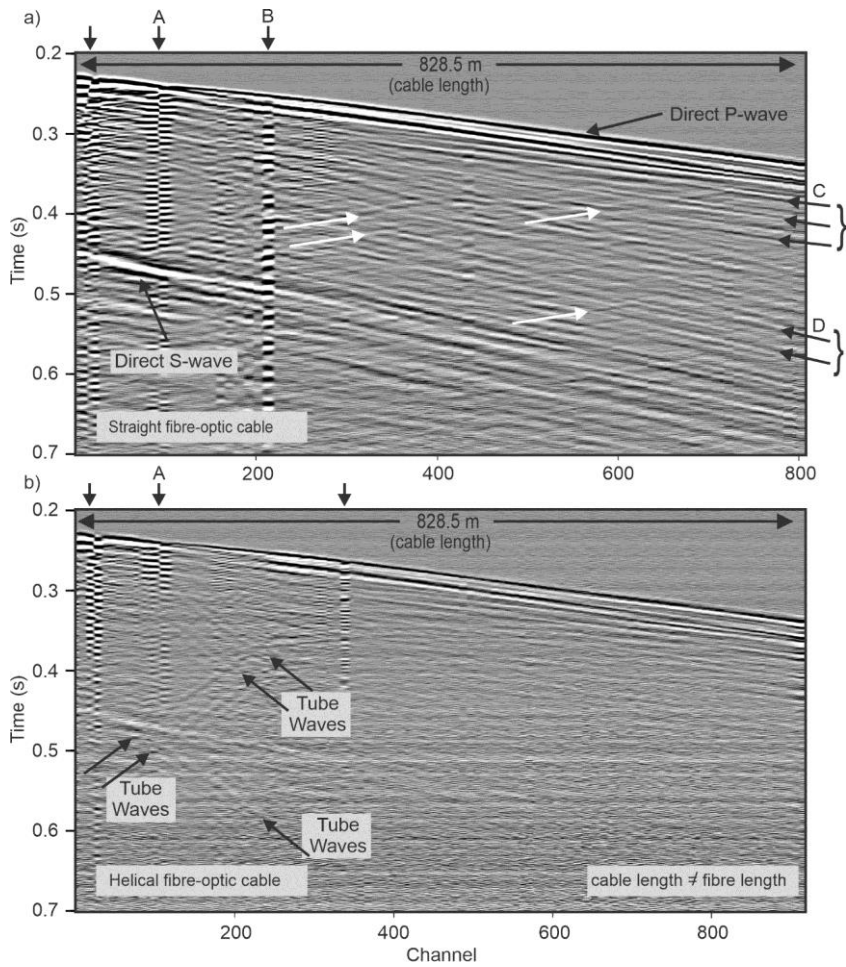
Acknowledgments

The authors would like to thank the Petroleum Technology Research Centre and Mitacs for funding in support of the modeling components of this research.

430

Commented [BG1]: This is ok for a response to reviewer but much for conclusions...

Commented [BG2]: This does not go into the conclusions. Adding "tube waves" into text is enough to clarify the point to an seismologist (ie. what is meant with surface waves).



435 **Figure 17622.** Comparison of field VSP data for a) straight fibre-optical cable and b) helically-wound fibre-optical cable. The helically-wound optical fibre has more channels than the straight fibre for the same length of cable due to the wrapping around the cable core (i.e., 925 channels for helically-wound cable versus 813 for the straight fibre-optical cable). Vertical arrows point to noisy channels indicating poor coupling. White arrows indicate up-going reflections. Arrows C and D point to events of the down-going wavefield with moveout of P-waves and S-waves, respectively. Events D arrive before the direct S-wave and are likely the result of P-to-S conversion at a lithological contact or fault zone. The same display gain was used for a) and b). Horizontal banding observed across all channels is optical noise. Modified from Bellefleur et al (2020).
440

Data Availability Statement

The data that support the findings of this study are available from the corresponding author upon request.

References

- 445 Bellefleur, G., Schetselaar, E., Wade, D., White, D., Enkin, R., and Schmitt, D.R.: Vertical seismic profiling using distributed acoustic sensing (DAS) with scatter-enhanced fiber-optic cable at the Cu-Au New Afton porphyry deposit, British Columbia, Canada; *Geophysical Prospecting*, 68, 313-333. <https://doi.org/10.1111/1365-2478.12828>, 2020.
- Daley, T. M., Pevzner, R., Dou, S., Correa, J., Robertson, M., Tertyshnikov, K., Wood, T., Ajo-franklin, J., Urosevic, M., Popik, D., Gurevich, B., Miller, D. E., White, D., Robertson, M., Cocker, J., Strudley, A., Craven, M., Worth, K., Harris, K.: *Advanced Monitoring Technology: DAS (Distributed Acoustic Sensing) at Otway and Aquistore*. IEA Greenhouse Gas Monitoring Network. Edinburgh, Scotland, 2016.
- 450 Daley, T.M., Freifeld, B.M., Ajo-Franklin, J., Dou, S., Pevzner, R., Shulakova, V., Kashikar, S., Miller, D.E., Goetz, J., Hennings, J. and Lueth, S.: Field testing of fiber-optic distributed acoustic sensing (DAS) for subsurface seismic monitoring. *The Leading Edge*, 32(6), pp.699-706, 2013.
- 455 Den Boer, J.J., Mateeva, A.A., Pearce, J.G., Mestayer, J.J., Birch, W., Lopez, J.L., Hornman, J.C. and Kuvshinov, B.N., Shell Oil Co.: Detecting broadside acoustic signals with a fiber optical distributed acoustic sensing (DAS) assembly. U.S. Patent 9,766,119, 2017.
- [Eaid, M., Li, J., and Innanen, K.A., 2018. Modeling the response of shaped-DAS fibres to microseismic moment tensor sources. 88th Annual International Meeting, SEG, Expanded Abstracts, 4698–4702.](#)
- 460 Folds, D.L. and Loggins, C.D.: Transmission and reflection of ultrasonic waves in layered media. *The Journal of the Acoustical Society of America*, 62(5), pp.1102-1109, 1977.
- Harris, K., White, D., Melanson, D., Samson, C., and Daley, T.: Feasibility of time-lapse VSP monitoring at the Aquistore CO₂ storage site using a distributed acoustic sensing system. *International Journal of Greenhouse Gas Control*, 50, 248-260. <http://doi.org/10.1016/j.ijggc.2016.04.016>, 2016.
- 465 Hartog, A.H.: *An introduction to distributed optical fibersensing*. CRC Press, Boca Raton, 472 p, 2018.
- Hornman, K.: Distributed Acoustic Sensing Cable for Surface Seismic. EAGE E-Lecture. Video retrieved from <https://www.youtube.com/watch?v=nCv5qytW1Y4>, 2015.
- [Innanen, K. \(2017\). Determination of seismic-tensor strain from Helical Wound Cable-Distributed Acoustic Sensing cable with arbitrary and nested-helix winds. In SEG Technical Program Expanded Abstracts 2017 \(pp. 926-930\). Society of Exploration Geophysicists.](#)
- 470 [Innanen, K. A., Lawton, D., Hall, K., Bertram, K. L., Bertram, M. B., & Bland, H. C. \(2019\). Design and deployment of a prototype multicomponent distributed acoustic sensing loop array. In SEG Technical Program Expanded Abstracts 2019 \(pp. 953-957\). Society of Exploration Geophysicists.](#)

475 Kuvshinov, B.N.: Interaction of helically wound fiber-optic cables with plane seismic waves. *Geophysical Prospecting*, 64(3), pp.671-688, 2016.

[Mateeva, A., Lopez, J., Potters, H., Mestayer, J., Cox, B., Kiyashchenko, D., ... & Detomo, R. \(2014\). Distributed acoustic sensing for reservoir monitoring with vertical seismic profiling. *Geophysical Prospecting*, 62\(4-Vertical Seismic Profiling and Microseismicity Frontiers\), 679-692.](#)

480 Miah, K., and Potter, D.K.: A review of hybrid fiber-optic distributed simultaneous vibration and temperature sensing technology and its geophysical applications. *Sensors* 2017, 17, 2511; doi:10.3390/s17112511, 2017.

Miller, D.E., Daley, T.M., White, D., Freifeld, B.M., Robertson, M., Cocker, J. and Craven, M.: Simultaneous acquisition of distributed acoustic sensing VSP with multi-mode and single-mode fiber-optic cables and 3C-geophones at the Aquistore CO2 storage site. *CSEG Recorder*, 41(6), 2016.

485 Mollahasani Madjdabadi, B.: Experimental Evaluation of a Distributed Fiber Optic Sensor for Mining Application, Doctoral dissertation, UWSpace, 2016.

[Ning, I. L. C., & Sava, P. \(2016\). Multicomponent distributed acoustic sensing. In *SEG Technical Program Expanded Abstracts 2016* \(pp. 5597-5602\). Society of Exploration Geophysicists.](#)

[Ning, I. L. C., & Sava, P. \(2018\). Multicomponent distributed acoustic sensing: Concept and theory. *Geophysics*, 83\(2\), P1-P8.](#)

490 [Ning, I. L. C. \(2019\). *Multicomponent Distributed Acoustic Sensing: Concept, Theory, and Applications*. Colorado School of Mines.](#)

Ranjan, P. and McColpin, G.: Fiber-Optic Sensing: Turning the Lights on Downhole. *The Digital Oil Field*, pp.34-37, 2013.

495 Riedel, M., Cosma, C., Enescu, N., Koivisto, E., Komminaho, K., Vaitinen, K., and Malinowski, M.: Underground vertical seismic profiling with conventional and fiber-optic systems for exploration in the Kylylahti polymetallic mine, eastern Finland. *Minerals*, 8, 538. <https://doi.org/10.3390/min8110538>, 2018.

500

505

510

515

520

525

Appendix A. A 2-D analytical approach to determine the dynamic strain of helically wound cable

For this two-dimensional (2-D) model, it is assumed that the seismic source is located far away from the location of the HWC. This assumption results in a plane wave propagating in the in X-Z plane (Figure A.1). The governing equation for a plane

530 sinusoidal wave in two-dimensional space is defined by following potential function:

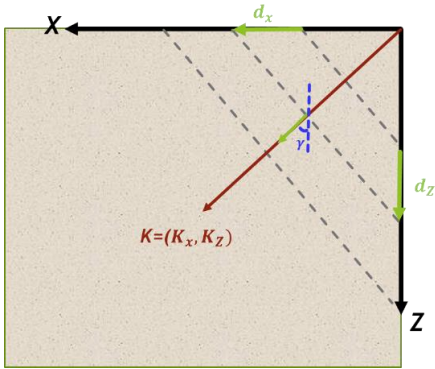
$$\varphi = A_0 \exp(i(K_x * x + K_z * z - \omega t)) \quad (\text{A.1})$$

Where A_0 is the initial amplitude of the seismic wave, k_x is the wavenumber in the x direction (rad/m), K_z is the wavenumber in the z direction (rad/m), ω is the angular frequency (rad/s), and t is the time (s).

The following relationship exists between displacement (u) and the potential function:

$$u = \nabla \varphi \quad (\text{A.2})$$

535 In order to define the compressional wave propagation equation as a function of incident angle (denoted by γ), we define the direction of ray path as a function of wave number (Fig. A.1).



540 **Figure A.1: The arrow is used to denote a ray and the dashed line is used to denote a wavefront. K indicates the direction of the ray. The angle γ is the incident angle**

According to Fig. A.2, the wavenumber can be defined as follows:

$$k = k_0(-\sin(\gamma), -\cos(\gamma)) \quad (\text{A.3})$$

Where k_0 is the initial wavenumber related to the initial source and γ is the incident angle the wavefront relative to the z -axis. In the above equation, the negative signs represent propagation in the negative quadrant of the coordinate system.

545 Under ideal assumptions (e.g., uniform density, uniform tension, no resistance to motion, small deflection, etc.), one can show that the displacement (u) satisfies the two-dimensional semi-infinite wave equation with free ends:

$$u_{tt} = C^2 \nabla^2 u = C^2 (u_{xx} + u_{yy}) \quad (\text{A.4})$$

Where C is a fixed non-negative real coefficient, and u_{tt} is $\frac{\partial^2 u}{\partial t^2}$

Assuming perfect plane wave propagation, stresses generated inside the medium far away from the acoustic source are obtained with the following equations:

$$\sigma_{xx} = (\lambda + 2\mu) \frac{\partial u_x}{\partial x} + \lambda \frac{\partial u_z}{\partial z} \quad (\text{A.5})$$

$$\sigma_{zz} = (\lambda + 2\mu) \frac{\partial u_z}{\partial z} + \lambda \frac{\partial u_x}{\partial x} \quad (\text{A.6})$$

Where μ and λ are shear modulus and lame constant, and σ_{xx} and σ_{zz} are stresses in x and z directions, respectively.

550 By substituting equations A.1 and A.2 into A.5 and A.6:

$$\sigma_{xx} = A_0((\lambda + 2\mu)(k_x^2) + \lambda(k_z^2)) \exp p(i(k_x * x + k_z * z - \omega t)) \quad (\text{A.7})$$

$$\sigma_{zz} = A_0((\lambda + 2\mu)(k_z^2) + \lambda(k_x^2)) \exp p(i(k_x * x + k_z * z - \omega t)) \quad (\text{A.8})$$

A plane acoustic wave is assumed to strike a multilayered media as shown in Figure A.2. The compressional wave originates from a source located in layer 1 and proceeds through the intervening layers to emerge into layer n+1. It should be noted that the HWC is in layer $\frac{n}{2} + 1$. The layers are assumed to have infinite extent in the z direction, and the plane wave incident upon layer 1 is assumed to lie in the X-Z plane, making the problem two-dimensional. In effect, concentric layers that would exist around a borehole in the true three-dimensional problem are represented as planar layers in this two-dimensional representation.

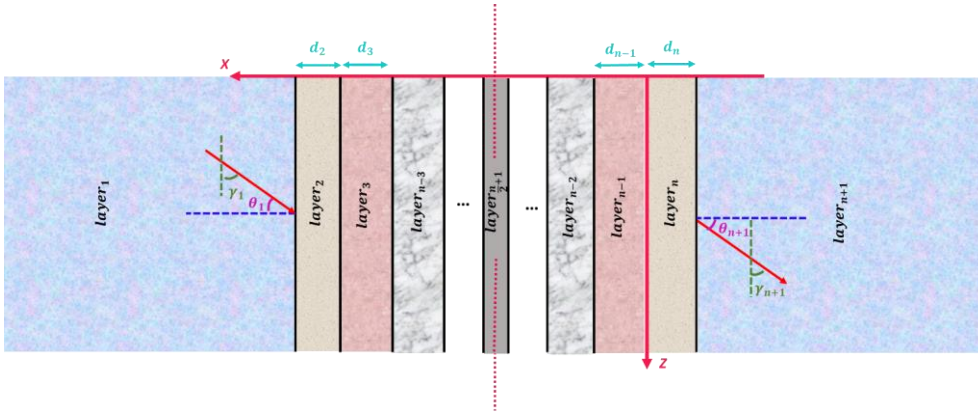


Figure A.2. Propagation of compressional waves from source (layer 1) to layer n+1 (After Folds and Loggins, 1977). In the scenario considered in this work, layer n/2+1 represents the borehole, which is a plane of symmetry in this 2D plane-strain model.

560 When the stratified medium consists of parallel solid plates, the equations for one section must be related to those of the adjacent section by proper boundary conditions used at interfaces between layers to satisfy continuity of normal (σ_{xx}) and shear stresses (σ_{xz}), and normal (u_x) and tangential displacements (u_z). Each layer (with layer number denoted by the index l) is considered linear elastic and isotropic if the following boundary conditions are satisfied:

$$u_x^l = u_x^{l+1} \quad (\text{A.9})$$

$$u_z^l = u_z^{l+1} \quad (\text{A.10})$$

$$\sigma_{xx}^l = \sigma_{xx}^{l+1} \quad (\text{A.11})$$

$$\sigma_{xz}^l = \sigma_{xz}^{l+1} \quad (\text{A.12})$$

At any layer, the displacements and stresses are given in terms of the following potential function [After 13]:

$$\varphi_l = (A_l \exp(i\alpha_l x) + B_l \exp(-i\alpha_l x)) \exp(i(\beta_l z - \omega t)) \quad (\text{A.13})$$

565 Where φ_l is the potential function for longitudinal waves, α_l is the x component of wavenumber, β is the z component of wavenumber, A_l is the amplitude of incident wave, and B_l the amplitude of reflected wave.

In equation A.13, $\alpha_l = k_l \sin\gamma_l$ and $\beta_l = k_l \cos\gamma_l$ are the x and z components of the wave vector, respectively. It should be noted that k_l is the wavenumber in layer l .

As shown in Figure A.2, the angle of the wave vector with the normal of the interface is θ . The following relationship exists
570 between the angle of the wavefront relative to the z-axis and the interface normal vector:

$$\gamma_1 = 90 - \theta_1 \quad (\text{A.14})$$

This yields:

$$\alpha_1 = k_1 \sin(\gamma_1) = k_1 \sin(90 - \theta_1) = k_1 \cos(\theta_1) \quad (\text{A.15})$$

$$\beta_1 = k_1 \cos(\gamma_1) = k_1 \cos(90 - \theta_1) = k_1 \sin(\theta_1) \quad (\text{A.16})$$

Clearly, based on Snell's equation, we must have:

$$k_1 \sin\theta_1 = k_2 \sin\theta_2 = \dots = k_{n-1} \sin\theta_{n-1} = k_n \sin\theta_n \quad (\text{A.17})$$

As shown in equation A.13, β is the same (according to Snell's law) for all layers. θ_l is the angle between the direction of the plane wave in layer l and the normal of interface.

575 At any point inside or on the boundaries of layer l , the displacements and stresses are defined as follows:

$$u_x^l = \frac{\partial \varphi_l}{\partial x} \quad (\text{A.18})$$

$$u_z^l = \frac{\partial \varphi_l}{\partial z} \quad (\text{A.19})$$

$$\sigma_{xx}^l = \lambda \left(\frac{\partial u_x^l}{\partial x} + \frac{\partial u_z^l}{\partial z} \right) + 2\mu \frac{\partial u_x^l}{\partial x} \quad (\text{A.20})$$

$$\sigma_{xz}^l = \mu \left(\frac{\partial u_x^l}{\partial z} + \frac{\partial u_z^l}{\partial x} \right) \quad (\text{A.21})$$

The displacements and stresses on the right-side interface of layer $n+1$ are obtained by substituting equation A.13 into equations A.20 and A.21 and using $l = n$, $x = h_n + \epsilon$ (where ϵ is infinitesimal):

$$h_n = d_1 + d_2 + \dots + d_{n-1} + d_n \quad (\text{A.22})$$

This yields:

$$\begin{bmatrix} \sigma_{xx}^{n+1} \\ \sigma_{xz}^{n+1} \end{bmatrix} = \begin{bmatrix} G_{n+1} N_{n+1} & G_{n+1} M_{n+1} \\ R_{n+1} N_{n+1} & -R_{n+1} M_{n+1} \end{bmatrix} \begin{bmatrix} A_{n+1} \\ B_{n+1} \end{bmatrix} \quad (\text{A.23})$$

with

$$N_{n+1} = \exp(i(\alpha_{n+1} h_n + \beta * z)) \quad (\text{A.24})$$

$$M_{n+1} = \exp(i(\beta * z - \alpha_{n+1} h_n)) \quad (\text{A.25})$$

$$R_{n+1} = -2 \mu_{n+1} \alpha_{n+1} \beta \quad (\text{A.26})$$

$$G_{n+1} = [(\lambda_{n+1} + 2\mu_{n+1})(-\alpha_{n+1}^2) + \lambda_{n+1}(-\beta^2)] \quad (\text{A.27})$$

580 Now just inside the n^{th} layer (e.g., at $= h_n - \epsilon$), the stresses are given as follows:

$$\begin{bmatrix} \sigma_{xx}^n \\ \sigma_{xz}^n \end{bmatrix} = \begin{bmatrix} G_n N_n & G_n M_n \\ R_n N_n & -R_n M_n \end{bmatrix} \begin{bmatrix} A_n \\ B_n \end{bmatrix} \quad (\text{A.28})$$

with

$$N_n = \exp(i(\alpha_n h_n + \beta * z)) \quad (\text{A.29})$$

$$M_n = \exp(i(\beta * z - \alpha_n h_n)) \quad (\text{A.30})$$

$$R_n = -2 \mu_n \alpha_n \beta \quad (\text{A.31})$$

$$G_n = [(\lambda_n + 2\mu_n)(-\alpha_n^2) + \lambda_n(-\beta^2)] \quad (\text{A.32})$$

Values in equation A.28 were obtained by substituting $n=1$ in equations A.17 and A.18.

Solving for the matrix of amplitude coefficients (A_{n+1} and B_{n+1}):

$$\begin{bmatrix} A_{n+1} \\ B_{n+1} \end{bmatrix} = \begin{bmatrix} 1/(2G_{n+1}N_{n+1}) & 1/(2R_{n+1}N_{n+1}) \\ 1/(2G_{n+1}M_{n+1}) & -1/(2R_{n+1}M_{n+1}) \end{bmatrix} \begin{bmatrix} \sigma_{xx}^{n+1} \\ \sigma_{xz}^{n+1} \end{bmatrix} \quad (\text{A.33})$$

585 Based on the boundary conditions described in A.11 and A.12, and substituting equation A.28 into the right hand side of equation A.29, the following equation is obtained:

$$\begin{bmatrix} A_{n+1} \\ B_{n+1} \end{bmatrix} = \begin{bmatrix} 1/(2G_{n+1}N_{n+1}) & 1/(2R_{n+1}N_{n+1}) \\ 1/(2G_{n+1}M_{n+1}) & -1/(2R_{n+1}M_{n+1}) \end{bmatrix} \begin{bmatrix} G_n N_n & G_n M_n \\ R_n N_n & -R_n M_n \end{bmatrix} \begin{bmatrix} A_n \\ B_n \end{bmatrix} \quad (\text{A.34})$$

As a result, the following relationship exists between the amplitude of layer $n+1$ and layer n :

$$\begin{bmatrix} A_{n+1} \\ B_{n+1} \end{bmatrix} = \begin{bmatrix} \binom{N_n}{2N_{n+1}} \binom{G_n}{G_{n+1}} + \binom{R_n}{R_{n+1}} & \binom{M_n}{2N_{n+1}} \binom{G_n}{G_{n+1}} - \binom{R_n}{R_{n+1}} \\ \binom{N_n}{2M_{n+1}} \binom{G_n}{G_{n+1}} - \binom{R_n}{R_{n+1}} & \binom{M_n}{2M_{n+1}} \binom{G_n}{G_{n+1}} + \binom{R_n}{R_{n+1}} \end{bmatrix} \times \begin{bmatrix} A_n \\ B_n \end{bmatrix} \quad (A.35)$$

The transformation matrix is named as E_i :

By considering:

$$\binom{N_n}{N_{n+1}} = \exp(ih_n(\alpha_n - \alpha_{n+1})) = S_{n+1} \quad (A.36)$$

$$\binom{N_n}{M_{n+1}} = \exp(ih_n(\alpha_n + \alpha_{n+1})) = V_{n+1} \quad (A.37)$$

$$\binom{M_n}{N_{n+1}} = \exp(-ih_n(\alpha_n + \alpha_{n+1})) = W_{n+1} \quad (A.38)$$

$$\binom{M_n}{M_{n+1}} = \exp(-ih_n(\alpha_n - \alpha_{n+1})) = J_{n+1} \quad (A.39)$$

$$E_{n+1} = \begin{bmatrix} \binom{S_{n+1}/2}{V_{n+1}/2} \binom{G_n}{G_{n+1}} + \binom{R_n}{R_{n+1}} & \binom{W_{n+1}/2}{J_{n+1}/2} \binom{G_n}{G_{n+1}} - \binom{R_n}{R_{n+1}} \\ \binom{V_{n+1}/2}{J_{n+1}/2} \binom{G_n}{G_{n+1}} - \binom{R_n}{R_{n+1}} & \binom{W_{n+1}/2}{J_{n+1}/2} \binom{G_n}{G_{n+1}} + \binom{R_n}{R_{n+1}} \end{bmatrix} = \begin{bmatrix} e_{11}^n & e_{12}^n \\ e_{21}^n & e_{22}^n \end{bmatrix} \quad (A.40)$$

$$\begin{bmatrix} A_{n+1} \\ B_{n+1} \end{bmatrix} = E_{n+1} \begin{bmatrix} A_n \\ B_n \end{bmatrix} \quad (A.41)$$

Application of the boundary condition at $x = h_n$ equates the velocities and stresses in layer n with those in layer n+1 at the interface, and the process used above can be repeated for each of the n-1 layers between n+1 and 1. Because of this, we can now write:

$$\begin{bmatrix} A_{n+1} \\ B_{n+1} \end{bmatrix} = [E_{n+1} E_n E_{n-1} \dots E_3 E_2] \begin{bmatrix} A_1 \\ B_1 \end{bmatrix} = \begin{bmatrix} F_{11} & F_{12} \\ F_{21} & F_{22} \end{bmatrix} \begin{bmatrix} A_1 \\ B_1 \end{bmatrix} \quad (A.42)$$

We have assumed that the layer n+1 extends to infinity, which results in the fact that there are no reflections inside layer n+1 ($B_{n+1} = 0$). In equation A.42, A_1 is the amplitude of the wave generated by the seismic source and it is a known parameter.

By having $B_{n+1} = 0$ and A_1 , we can estimate B_1 and A_{n+1} with the following equations:

$$B_1 = -(F_{21}/F_{22})A_1 \quad (A.43)$$

$$A_{n+1} = (F_{11})A_1 + (F_{12})B_1 \quad (A.44)$$

595 By knowing A_1 and B_1 , it is possible to calculate the amplitude of incident and reflected waves inside each layer. As a result,
by replacing these values inside equation A.13, we are able to calculate stresses and displacements for each layer.

Strains can be calculated directly from displacements with the following relationships:

$$\epsilon_{xx}^n = \partial u_{xx}^n / \partial X \quad (\text{A.45})$$

$$\epsilon_{zz}^n = \partial u_{zz}^n / \partial Z \quad (\text{A.46})$$

Following the two-dimensional dynamic strain response on the HWC as represented by the coordinate system in the right-
hand side of Fig. 2b, ϵ_{xx} is equal to radial strain (ϵ_{rr}) and ϵ_{zz} is equal to longitudinal strain (ϵ_{ll}) (Fig. 2b). As a result, fiber

600 strain (ϵ_{zz}) is calculated as follows:

$$\epsilon_{zz(\text{Fiber})} = \epsilon_{ll(\text{Cable})} \cos^2 \alpha + \epsilon_{rr(\text{Cable})} \sin^2 \alpha \quad (\text{A.47})$$

605

610

615

620

625

630

Appendix B. A pseudocode for 2-D analytical approach

635 H=0;

Foreach $Theta_1 = 0 \dots M$ **do**

Foreach $layer\ n=1 \dots n$ **do**

$$K_n = (2 * \pi * Freq) / C_{p_n}$$

$$Theta_n = \text{asin}\left(\frac{K_n}{K_1}\right) * \sin(Theta_1)$$

640 $Alpha_n = K_n * \cos(Theta_n)$

$$Beta_n = K_n * \sin(Theta_1)$$

If $n == (n + 1/2)$ **then** _____ // The Cable is located in the layer of $((n+1)/2)$

$$H_n = H + Diameter_n$$
 else

$$H_n = H + Diameter_n / 2$$

645 **endif**

$$N_n = \exp(1i * (H_n * Alpha_n + Beta_n * z))$$

$$M_n = \exp(1i * (-H_n * Alpha_n + Beta_n * z))$$

$$R_n = -2 * \mu_n * Alpha_n * Beta_n$$

$$G_n = (-\lambda_n + 2 * \mu_n) * (Alpha_n^2) - (\lambda_n) * (Beta_n^2)$$

650 **If** $n > 1$ **then**

$$S_n = \exp(1i * H_{n-1} * (Alpha_{n-1} - Alpha_n))$$

$$V_n = \exp(1i * H_{n-1} * (Alpha_{n-1} + Alpha_n))$$

$$W_n = \exp(-1i * H_{n-1} * (Alpha_{n-1} + Alpha_n))$$

$$J_n = \exp(-1i * H_{n-1} * (Alpha_{n-1} - Alpha_n))$$

655 Array $E_n[2]$ [2]

$$E_n[0][0] = \left(\frac{S_n}{2}\right) * \left(\left(\frac{G_{n-1}}{G_n}\right) + \left(\frac{R_{n-1}}{R_n}\right)\right)$$

$$E_n[0][1] = \left(\frac{W_n}{2}\right) * \left(\left(\frac{G_{n-1}}{G_n}\right) - \left(\frac{R_{n-1}}{R_n}\right)\right)$$

$$E_n[1][0] = \left(\frac{V_n}{2}\right) * \left(\left(\frac{G_{n-1}}{G_n}\right) - \left(\frac{R_{n-1}}{R_n}\right)\right)$$

$$E_n[1][1] = \left(\frac{I_n}{2}\right) * \left(\left(\frac{G_{n-1}}{G_n}\right) + \left(\frac{R_{n-1}}{R_n}\right)\right)$$

660 **Endif**

End

$$F = E_n * E_{n-1} * \dots * E_2$$

$$B_1 = -\left(\frac{F[1][0]}{F[1][1]}\right) * A_1 \quad // B_1 \text{ is the amplitude of reflected wave in the first layer}$$

$$A_n = F[0][0] * A_1 + F[0][1] * B_1 \quad // A_n \text{ is the amplitude of transmitted wave in the last layer}$$

665 $L = E_{(n+1)/2} * E_{\left(\frac{n+1}{2}\right)-1} * \dots * E_2$

$$B_{(n+1)/2} = L[1][0] * A_1 + F[1][1] * B_1 \quad // B_{(n+1)/2} \text{ is the amplitude of reflection wave in the cable layer}$$

$$A_{(n+1)/2} = L[0][0] * A_1 + F[0][1] * B_1 \quad // A_{(n+1)/2} \text{ is the amplitude of refraction wave in the cable layer}$$

$$\varepsilon_{xx(n+1)/2} = \left(\frac{Alpha_{(n+1)/2}}{2}\right)^2 * \left(-\frac{A_{n+1}}{2} * \exp\left(1i * Alpha_{(n+1)/2} * H_{(n+1)/2}\right) - \frac{B_{n+1}}{2} * \exp\left(-1i * Alpha_{(n+1)/2} * H_{(n+1)/2}\right)\right) * \exp\left(1i * Beta_{(n+1)/2} * z\right) \quad // \varepsilon_{xx(n+1)/2} \text{ and } \varepsilon_{zz(n+1)/2} \text{ are calculated strains in the cable layer}$$

$$H_{(n+1)/2} * \exp\left(1i * Beta_{(n+1)/2} * z\right) \quad // \varepsilon_{xx(n+1)/2} \text{ and } \varepsilon_{zz(n+1)/2} \text{ are calculated strains in the cable layer}$$

670 $\varepsilon_{zz(n+1)/2} = -\left(\frac{Beta_{(n+1)/2}}{2}\right)^2 * \left(\frac{A_{n+1}}{2} * \exp\left(1i * Alpha_{(n+1)/2} * H_{(n+1)/2}\right) + \frac{B_{n+1}}{2} * \exp\left(-1i * Alpha_{(n+1)/2} * H_{(n+1)/2}\right)\right) * \exp\left(1i * Beta_{(n+1)/2} * z\right)$

$$H_{(n+1)/2} * \exp\left(1i * Beta_{(n+1)/2} * z\right)$$

End

Formatted: Font: Cambria Math